Uncertainty in 21st Century Projections of the Atlantic Meridional Overturning Circulation in CMIP3 and CMIP5 models

A. Reintges (corresponding author), T. Martin, M. Latif
GEOMAR Helmholtz Centre for Ocean Research Kiel
Düsternbrooker Weg 20, 24105 Kiel, Kiel, Germany
e-mail: areintges@geomar.de
telephone: +49 431 600-4007
fax: +49 431 600-4052

N. S. Keenlyside
Geophysical Institute and Bjerknes Centre, University of Bergen
Allégaten 70, 5020 Bergen, Norway

Uncertainty in 21st Century Projections of the Atlantic Meridional Overturning Circulation in CMIP3 and CMIP5 models

Annika Reintges, Thomas Martin, Mojib Latif and Noel S. Keenlyside

Abstract

Uncertainty in the strength of the Atlantic Meridional Overturning Circulation (AMOC) is analyzed in the Coupled Model Intercomparison Phase 3 (CMIP3) and Phase 5 (CMIP5) projections for the 21st century; and the different sources of uncertainty (scenario, internal and model) are quantified. Although the uncertainty in future projections of the AMOC index at 30°N is larger in CMIP5 than in CMIP3, the signal-to-noise ratio is comparable during the second half of the century and even larger in CMIP5 during the first half. This is due to a stronger AMOC reduction in CMIP5. At lead times longer than a few decades, model uncertainty dominates uncertainty in future projections of AMOC strength in both the CMIP3 and CMIP5 model ensembles. Internal variability significantly contributes only during the first few decades, while scenario uncertainty is relatively small at all lead times. Model uncertainty in future changes in AMOC strength arises mostly from uncertainty in density, as uncertainty arising from wind stress (Ekman transport) is negligible. Finally, the uncertainty in changes in the density originates mostly from the simulation of salinity, rather than temperature. High-latitude freshwater flux and the subpolar gyre projections were also analyzed, because these quantities are thought to play an important role for the future AMOC. The freshwater input in high latitudes is projected to increase and the subpolar gyre is projected to weaken. Both the freshening and the gyre weakening likely influence the AMOC by causing anomalous salinity advection into the regions of deep water formation. While the high model uncertainty in both parameters may explain the uncertainty in the AMOC projection, deeper insight into the mechanisms for AMOC is required to reach a more quantitative conclusion.

Keywords: Atlantic Meridional Overturning Circulation (AMOC), North Atlantic ocean, uncertainty, climate projections

1. Introduction

The AMOC (Ganachaud and Wunsch 2003; Srokosz et al. 2012) is characterized by a northward flow of warm, salty water in the upper layers of the Atlantic, and a southward return flow of colder water in the deep Atlantic (Dickson and Brown 1994). It transports a substantial amount of heat from the tropics and Southern Hemisphere toward the North Atlantic, where the heat is then transferred to the atmosphere. The mild climate of Northern Europe is in part a consequence of this heat supply. Changes in the AMOC are thought to have a profound impact on many aspects of the global climate system. For example, the Atlantic Multidecadal Oscillation or Variability (AMO/V), a coherent pattern of multidecadal variability in surface temperature centered on the North Atlantic Ocean, is linked to the AMOC in climate models (Knight et al. 2005; Zhang and Delworth 2006). Further aspects that are hypothesized to be related to the AMOC are: observed decadal variability in the air-sea heat exchange over the North Atlantic (Gulev et al. 2013), continental summertime climate of both North America and western Europe (Sutton and Hodson 2005), Atlantic hurricane activity, Sahel rainfall and the Indian Summer Monsoon (Zhang and Delworth 2006).

Direct measurements of AMOC strength from the RAPID-MOCHA array at 26.5°N reveal a decline since 2004 (McCarthy et al. 2012, Smeed et al. 2014): During 2008-2012 the AMOC was 2.7 Sv (1 Sv = 10^6 m³/s) weaker than during 2004-2008. Because of the relatively short observational record it is unclear whether this decline is just a short-term fluctuation or part of a long-term trend. However, records show that density in the Labrador Sea began to fall in the late 1990s, and this may suggest more persistent AMOC weakening (Robson et al. 2014).

Roberts et al. (2014) suggest that this decline could be due to internal variability. However, they also stress that the CMIP5 models generally underestimate the interannual variability of the AMOC. This may be also the case at decadal timescales due to salinity biases, as recently discussed by Park et al. (2016).

How will the AMOC evolve during the next decades and the whole 21st century? Future changes in the AMOC will result from both internal and external processes of the climate system. On the one hand, in control integrations with fixed external forcing many climate models simulate strong internal AMOC variability on decadal to multi-decadal and even centennial timescales (e.g., Danabasoglu 2008; Latif et al. 2004; Knight et al. 2005; Park and Latif 2008; Delworth and Zeng 2012; see Latif and Keenlyside 2011 for a review). On the other hand, external forcing such as anthropogenic emissions of long-lived greenhouse gases (GHGs) driving global warming may also influence the future AMOC, as has been shown in numerous modeling studies. The internal decadal to centennial AMOC variability will superimpose and hinder detection of a potential anthropogenic AMOC signal, which evolves on similar timescales.

A wide variety of mechanisms have been put forward for how global warming will influence AMOC. Global warming in response to enhanced atmospheric GHG concentrations will be accompanied by changes in the vertical temperature and salinity profiles in the ocean. The meridional structure of these changes will affect the meridional oceanic density contrast, which has been suggested to be correlated with the AMOC strength (e.g., Thorpe et al. 2001). Additionally to the importance of these processes, a large number of theoretical and modeling studies pointed out the control of the AMOC by a number of internal ocean processes (as reviewed by Kuhlbrodt et al., 2007). Delworth et al. (1993) suggested an interdecadal oscillation caused by the interaction between the AMOC and the horizontal gyre circulation. The influence of the subpolar gyre on the AMOC was supported by a multi-model study of Ba et al. (2014). Further, a remote influx at the depth of the overturning, due to changes in the

Southern Ocean wind stress and Antarctic Bottom Water (AABW) formation, might counteract the effect of changes in the meridional density gradient (de Boer et al. 2010). Shakespeare and Hogg (2012) found that the AMOC scales linearly with both the Southern Ocean wind stress and northern buoyancy flux. Gnanadesikan (1999) pointed out that the difference between northern sinking and upwelling in the Southern Ocean are balanced by changes in the low-latitude isopycnal depth. The rate of sinking in the north depends on the parameterization of vertical mixing. Sijp et al. (2006) derived the importance of isopycnal mixing in models, because it does not require a strong vertical instability. They argue that buoyancy-driven convection overestimates the sensitivity of deep water production against surface freshwater fluxes. The temporal and spatial interactions of all these processes determine the mean state, the internal variability and the externally caused changes of the AMOC intensity. Finally, the relative importance of these processes is unknown under changing climate conditions, and might be different from the importance of the processes that determine the mean state in climate model projections. Thus there are major uncertainties in how AMOC will respond to global warming.

Climate models generally predict a weakening of the AMOC during the 21st century when forced by enhanced levels of GHG concentrations, but large uncertainties exist (e.g., Schmittner et al. 2005). This uncertainty can be conceptually decomposed into three components (Hawkins and Sutton 2009, Hawkins and Sutton 2011): First, the future GHG emissions are unknown. The climate models are therefore run under different GHG scenarios, leading to the so-called scenario uncertainty. Second, a large uncertainty exists, even under identical GHG forcing (Schmittner et al. 2005). One reason for this uncertainty is internal stochastically driven AMOC fluctuations (e.g., Park and Latif 2012, Mecking et al. 2014). This kind of uncertainty is called internal variability. Third, there is uncertainty arising from model systematic error that is called model uncertainty, also sometimes termed response uncertainty. Model uncertainty might originate from the ocean, the atmospheric or the sea ice components of the coupled models, since all three influence the surface fluxes of heat, freshwater and momentum that drive the AMOC. For example, the large mean biases in the North Atlantic found in the most climate models (Wang et al. 2014) lead to errors in the northward path of saline waters, potentially affecting internal variability and the model response to enhanced GHG concentrations.

The main purpose of this study is to investigate the consistency between the CMIP models with regard to projecting 21st century GHG-forced AMOC change and to identify the origin of uncertainties. As the complex processes controlling AMOC are poorly understood, a full mechanistic understanding of future projections in AMOC remains a major challenge in climate research and is beyond the scope of this paper. The focus of this paper is rather to examine a few key variables that have been identified to be of relevance for the AMOC. We follow the methodology outlined by Hawkins and Sutton (2009) and quantify as function of lead time the three individual contributions – scenario, internal, and model – to the total AMOC projection uncertainty. We show that, in both the CMIP3 and CMIP5 model ensembles, model uncertainty dominates AMOC projections for the 21st century at lead times beyond a few decades. This paper is organized as follows. In Section 2, we describe the data and the methodology used in this study. We present the results of the AMOC projection uncertainty analysis in Section 3. The results are summarized in Section 4.

2. Data and methodology

Data

We have used climate model simulations from the World Climate Research Programme's (WCRP's) Coupled Model Intercomparison Project phase 3 (CMIP3; Table 1) (Meehl et al. 2007a) and phase 5 (CMIP5; Table 2) (Taylor et al. 2012). The multi-model datasets are provided by the Program for Climate Model Diagnosis and Intercomparison (PCMDI). From

CMIP3 we used the 20C3M data for the 20th century and the IPCC SRES scenarios A1B, A2, and B1 for the 21st century. The scenario B1 comprises the weakest, A1B a moderate, and A2 the strongest radiative forcing. For the CMIP5 analysis, we used the 'historical' data representing the 20th century and the RCP4.5 and RCP8.5 scenarios for the 21st century. These two scenarios are core experiments of CMIP5, and thus were performed with virtually all participating models. The scenario with higher radiative forcing is RCP8.5. Combining the 20th– and the 21st-century scenarios our analysis covers the period 1850-2100. The CMIP models provide the depth profile of the meridional overturning streamfunction in the Atlantic, defined in z-coordinates and as function of latitude. From this variable we also computed the indices of the AMOC strength by taking the maximum in the vertical for a given latitude. This is a common measure of the AMOC strength. In the CMIP3 ensemble, the mean depth of the overturning streamfunction maximum at 30°N during the years 1970-2000 is 1,115 m with an inter-model standard deviation of 519 m and in the CMIP5 ensemble, 1,036 m with an inter-model standard deviation of 140 m. These numbers seem to be reasonable when compared to the observed profile at 26°N which also depicts a maximum at roughly 1,100 m (Smeed et al. 2014). For our analysis we use the latitudes 30°N and 48°N, because in most models 30°N matches the center of the overturning cell quite well, whereas 48°N is a location with large variability. Furthermore, zonal mean salinity and potential temperature profiles are analyzed in this study. These were also used to calculate density changes. We also investigate the Arctic and North Atlantic freshwater fluxes (WFO) from 0°-90°N integrated over different areas. WFO includes the effects of evaporation, precipitation, river runoff, and sea ice changes. Finally, we compute the uncertainties also for the subpolar gyre index, which is derived from the barotropic streamfunction.

For most of the variables, we perform most of our analysis separately on both CMIP3 and CMIP5 data. The total number of models in the CMIP3 database is smaller than that of CMIP5

(Tables 1 and 2). Of course, the models are not entirely independent of each other; some models originate from the same modeling center and some share the same model components (Masson and Knutti 2011). Therefore, the model uncertainty derived from the model ensemble used here could be biased. To test this, we repeated the analyses with a smaller ensemble by removing those models that have a setting too close to another model or behave too similar regarding one or more variables. Our main findings remained qualitatively unchanged in these tests. Finally, one should note that the forcing used in the CMIP3 and CMIP5 integrations is similar but not identical; this is discussed below in the result section.

Statistical method

Uncertainty is a term used in different fields. In this study, uncertainty reflects the spread between ensemble members within the CMIP projection of future climate. The CMIP data offer a wide range of results for historic simulations and future climate projections. As the true path of AMOC strength is unknown, it is difficult to evaluate the quality of the model-based future projections. To define uncertainty we derive variances from inter-simulation differences. Total uncertainty may not be decomposed into a linear combination of individual sources of uncertainty, as cross terms may exist (i.e., variance of one component might depend on one of the other factors). For example, the sensitivity to a specified forcing scenario and the internal variability could be related and be model-dependent. However, here we are not interested in the uncertainty of individual model projections, but only in integral quantities computed over the complete model ensemble. Furthermore, we analyzed the cross terms and found them to be sufficiently small not to impact the major conclusions of this work, and thus they will be neglected in the remainder of the analysis.

For the quantification of the three sources of uncertainty we basically follow the approach suggested by Hawkins and Sutton (2009), although we adapted the method for calculating the internal variability. A more complete framework has been proposed, but it was shown to give similar results when analyzing CMIP3 models (Yip et al. 2011). For a given scalar variable of our analysis (e.g. AMOC strength or density at a fixed position) we define the term model projections $X(m,s,t)$ as the climate realizations dependent on time, t, and obtained from various CMIP models, m, and different 21st century forcing scenarios, s. The projections $X(m,s,t)$ are split into a long-term variability component, representing the response to external forcing $X_f(m,s,t)$, and a short-term residual $\varepsilon(m,s,t)$, representing internal fluctuations:

$$X(m,s,t) = X_f(m,s,t) + \varepsilon(m,s,t) \qquad (1).$$

A model response to external forcing is typically computed as the mean across a large ensemble of experiments performed with that model prescribing identical external forcing but started from different initial conditions. In the absence of such data we estimate the external forced AMOC component, $X_f(m,s,t)$, by a 4th order polynomial fit computed over the full time series. A 4th-order polynomial is chosen as it captures the non-linear response of AMOC to external forcing that includes the reduced weakening of the AMOC at the end of the 21st century found in several models. Our main conclusions remain insensitive to this choice, as shown by repeating the uncertainty analysis of the AMOC index at 30°N from the CMIP5 ensemble with polynomial orders from 2, 3, and 5 (see supplementary material).

Then, from the long-term fit $X_f(m,s,t)$ we calculate a long-term anomaly $x_f(m,s,t)$ relative to the initial value $i(m,s)$, which is the average over the years 1970 to 2000:

$$X_f(m,s,t) = i(m,s) + x_f(m,s,t) \quad (2).$$

Three sources of uncertainty are distinguished. The calculation of these components involves taking the variance over the respective component. In our equations, we use a variance operator defined as follows:

$$VAR_d(p) = \frac{1}{N_d - 1} \sum_d \left(p - \frac{1}{N_d} \sum_d p \right)^2 \quad (3).$$

Here, p is any parameter for which the variance is computed in the dimension d.

The first source of uncertainty is the internal variability and defined as

$$I = \frac{1}{N_s}\sum_s \frac{1}{N_m}\sum_m VAR_t\left(\varepsilon(m,s,t)\right) \quad (4).$$

N_s and N_m are the numbers of scenarios and models, respectively. Internal variability is represented by the variance of the residual *ε(m,s,t)* over time, averaged over all models and all scenarios. Therefore, internal variability is given as one value.

The second source of uncertainty is the model uncertainty and defined as

$$M(t) = \frac{1}{N_s}\sum_s VAR_m(\,x_f(m,s,t)) \quad (5).$$

It represents the spread between the different model realizations. Here, we take the variance of the long-term anomaly $x_f(m,s,t)$ over the model dimension *m*, and then average over the different scenarios. According to our definition the internal variability includes only frequencies on inter-annual or decadal timescales. Since the AMOC exhibits long-term variability (e.g. the Atlantic Multidecadal Variability, AMV), which cannot be completely filtered out by the polynomial fit, the model uncertainty contains also some uncertainty due to internal variability.

The third source of uncertainty is the scenario uncertainty and defined as

$$S(t) = VAR_s\left(\frac{1}{N_m}\sum_m x_f(m,s,t)\right) \quad (6).$$

It represents the spread of the long-term anomaly $x_f(m,s,t)$, averaged over all models for each scenario. The estimate of the total uncertainty *T(t)* is defined as the sum of the internal, model and scenario uncertainty. Finally, we calculated the signal-to-noise ratio *SNR(t)* with a two-sided confidence level c:

$$SNR(t) = \frac{G(t)}{q_{\frac{c}{2}}\sqrt{T(t)}} \qquad (7).$$

Here $q_{\frac{c}{2}}$ is the $\frac{c}{2}$th quantile of the standard normal distribution. In this analysis, a confidence level of 90% is used. *G(t)* is the mean signal

$$G(t) = \frac{1}{N_s}\sum_{s}\frac{1}{N_m}\sum_{m} x_f(m,s,t) \quad (8)$$

which is estimated from the averaged model fit x_f considering all models and scenarios. A signal-to-noise ratio *SNR(t)* larger than unity indicates that the mean climate signal *G(t)* exceeds the amplitude of the noise and is therefore detectable. The uncertainty analysis below is based on decadal means.

3. Results

AMOC

The ensemble-mean of the late 20th century (1970-2000) Atlantic meridional overturning streamfunction depicts a distinct maximum just below 1000 m in the region 30°N-45°N in both the CMIP3 (Fig. 1a) and CMIP5 (Fig. 1d) model ensemble. The North Atlantic Deep Water (NADW) cell reaches down to roughly 3000 m, which is shallower than what observations suggest (McCarthy et al. 2012). We note, however, that the vertical extent of the cell varies from model to model. The overall structure of the ensemble-mean is rather similar in the two CMIP ensembles, but the mean strength of the overturning is considerably stronger in the CMIP5 ensemble. The vertical maximum at 26°N is close to 19 Sv in the CMIP5 ensemble, as opposed to 16 Sv in the CMIP3 ensemble. These numbers are closer to the observations obtained from the RAPID array at 26°N, indicating AMOC strength of about 17.5 Sv during the years 2004-2012 (Smeed et al. 2014). Decadal variability, however, may be large. Furthermore, it must be noted that the spread among the models is huge and for the vertical maximum at 26°N the models provide a range of 12.1 - 29.7 Sv in CMIP5 and 6.6 – 27.4 Sv in CMIP3. The ensemble-mean AABW cell, which is located below the NADW cell, is rather similar in both ensembles.

The ensemble-mean projected change in the Atlantic meridional overturning streamfunction for the end of the 21st century (2090-2100 relative to 1970-2000) is shown in Fig. 1b and 1e. A clear weakening of the NADW cell is seen in both ensembles, with the strongest change in the streamfunction near 40°N, while there is a slight strengthening of the AABW cell. The spatial pattern of the change is rather similar, but the magnitude is considerably stronger in the CMIP5 ensemble. In both ensembles, the maximum reduction occurs below the absolute maximum of the ensemble-mean streamfunction, which results in a shallower NADW cell. We note that although the radiative forcing is roughly comparable in the two ensembles, it is not identical. For example, the changes in global annual-mean surface air temperature by the year 2100 depending on the scenario are: in CMIP3 1.8°C (B1), 2.8°C (A1B), 3.6°C (A2) relative to 1980-1999 (Meehl et al. 2007b); and in CMIP5 1.9°C (RCP4.5), 4.1°C (RCP8.5) relative to 1986-2005 (Collins et al. 20013). The relative change of the overturning is comparable and amounts to about a 25-30% reduction by the end of the 21st century. The stronger absolute weakening in the CMIP5 ensemble causes a larger signal-to-noise ratio in the CMIP5 ensemble with a maximum of about 1.5 (Fig. 1f) as opposed to about 1 in the CMIP3 ensemble (Fig. 1c). A signal-to-noise ratio of unity denotes the significance limit with 90%-confidence. Thus, a value of 1.5 is indicative of a highly significant and detectable change.

In the following, we take the maxima of the streamfunction at 30°N and 48°N as indices for the AMOC strength. The 30°N index is close to the center of the overturning cell and also is a good indicator for a large meridional scale of the cell. Additionally, we select an AMOC index at 48°N that is close to the northern edge of the overturning cell and displays higher variability than the index at 30°N. We show the individual projections at 30°N for both CMIP3 (Fig. 2a) and CMIP5 (Fig. 2d), for each model and for each scenario, with a 10-year running mean applied to aid visualization (but all uncertainty analysis is performed on decadal means). A large spread is obvious in the long-term AMOC projections at 30°N in the CMIP3 and CMIP5 ensembles. In both ensembles, the largest contribution to the total uncertainty is related to the model differences (blue) at almost all lead times (Fig. 2b, 2e); while the contribution from the internal variability (red) is rather small at all lead times. Although climate models may underestimate the interannual variability of the AMOC (Roberts et al. 2014), model uncertainty would still dominate by far even if the internal variability component was twice as large as estimated here. Similarly, model uncertainty dominates for any reasonable choice of polynomial order used to identify the forced component (see supplementary material). By 2100, the contribution of scenario uncertainty (green) is substantial (about 20%) in the CMIP5 ensemble, but is rather small in the CMIP3 ensemble. This may be partly related to the larger range of radiative forcing and to larger model sensitivity in CMIP5. Independently of this, the main conclusion is unchanged as we move from CMIP3 to CMIP5: the model uncertainty is by far the largest contribution to the total uncertainty in the AMOC projections for the 21st century at lead times of several decades and beyond. Both CMIP ensembles yield a relatively large signal-to-noise ratio for the AMOC change at 30°N (red line in Fig. 2c and 2f) at lead times beyond a few decades. The signal-to-noise ratio tends to diminish at longer lead times. This reflects the dominance of the model uncertainty compared to the projected AMOC reduction. The signal-to-noise ratio is generally larger at 30°N than at 48°N (blue line in Fig. 2c and 2f), which indicates a greater detectability of an anthropogenic signal in the subtropics compared to the mid-latitudes.

Although geostrophic transport dominates the time-mean AMOC, both geostrophic and Ekman transports are important in explaining the AMOC variability. We derived the Ekman contribution to the AMOC model uncertainty at 30°N from the wind stress curl field (Visbeck et al. 2003). The Ekman component of model uncertainty is shown together with the remaining model uncertainty and the other two uncertainty sources in Fig. 3. The Ekman contribution (yellow) is rather small and becomes comparable to the AMOC uncertainty due to the internal variability by the end of the 21st century. The Ekman uncertainty is thus, in both model ensembles, only a marginal contributor to the total AMOC projection uncertainty.

As scenario uncertainty plays only a minor role compared to model uncertainty, we will focus on only one scenario per model ensemble during all following analyses. We choose scenarios with a moderate radiative forcing: SRES A1B for CMIP3 and RCP4.5 for CMIP5. One should keep in mind that the global-mean surface air temperature change by the year 2100 is larger in A1B (2.8°C relative to 1980-1999) than in RCP4.5 (1.9°C relative to 1986-2005).

We benchmark the relationships of the AMOC to several parameters that have been previously identified as relevant, for both CMIP3 and CMIP5 ensembles as follows: Table 3 lists correlations computed across the model ensembles between the AMOC index at 30°N and these parameters (see table caption for definitions). For the correlations time averages over 1970-2000 or 2070-2100 are used. The correlations are not computed in the time- but in the model-domain (detailed equations are given in the supplementary material). We use all available models for these correlations. We did not remove outliers because there are no uniform metrics that define an outlier reliably. Sometimes one model seems to perform well for one variable but not for a different one. The strongest and significant correlation with the mean AMOC index at 30°N in the model ensemble for both periods is found for the subpolar gyre (SPG) index ($r_{historical}$ = 0.87 and $r_{RCP4.5}$ = 0.88). The SPG index is defined here as the minimum of the barotropic streamfunction in the region 60°W-15°W / 45°N-65°N, and multiplied by -1. The SPG mean state is negative in the barotropic streamfuction, indicating anti-clockwise circulation, and our SPG index hence reflects the strength of this anti-clockwise circulation. Also the Atlantic mean meridional depth-integrated density difference (MDD) is significantly related to the AMOC index ($r_{historical}$ = 0.75 and $r_{RCP4.5}$ = 0.86). A separation of MDD into salinity- and temperature-driven components (MDD_{sal} and MDD_{temp}) suggests that salinity dominates this relationship, especially when the correlation of the differences is compared. Scatter plots between the AMOC index and density gradients from the CMIP3 and CMIP5 models (Fig. 4) show that a strong AMOC goes along with a large meridional density gradient. This relationship is in agreement with studies that incorporate simple box models of the Stommel type (Stommel 1961). However, we want to stress that the variability of the AMOC and general ocean circulation in a climate model is driven by more complex ocean-atmosphere interactions. The near-linear relationship between the AMOC index and the meridional density gradient (Fig. 4a) is primarily caused by the changes in salinity (Fig. 4c). Due to geostrophy, we also expect a dependence of the AMOC strength on the zonal density gradient (Sijp et al. 2012). However, the link between the AMOC index and the zonal density difference (ZDD) is weaker ($r_{historical}$ = 0.63 and $r_{RCP4.5}$ = 0.62; Fig. 4b) than the link to MDD, and changes in ZDD are only weakly related to projected changes in AMOC strength (r=0.16). Further parameters that exhibit no strong correlation to the AMOC index are the northward Ekman transport at the southern border of the Atlantic (50°S) and the pycnocline depth.

As MDD appears to be closely related to the projected AMOC changes, a similar correlation analysis was performed to identify the factors most related to the MDD (Table 4). The freshwater flux at the ocean surface (WFO) seems to play a role in determining the mean meridional density gradient. We also considered integrating the freshwater flux over time for this analysis. However, this did not affect the relative importance of model uncertainty and internal variability, nor the signal-to-noise ratio. We find negative correlations with WFO_{Arctic} (integrated over the Arctic; $r_{historical}$ = -0.62 and $r_{RCP4.5}$ = -0.48) and WFO_{30-50N} (integrated over the Atlantic 30°-50°N; $r_{historical}$ = -0.77 and $r_{RCP4.5}$ = -0.71). But for the difference between the two periods there is no relationship ($r_{diff.}$ = -0.03 / -0.10). We point out that the validity of our results in Tables 3 and 4 is limited. Low correlations with the AMOC index may be biased by strong model uncertainties. For example, the weak link of the ZDD with AMOC does not necessarily imply that the former is unrelated to AMOC strength or change. Instead, this may reflect differences in model dynamics. Furthermore, correlation analysis cannot identify causal links. However, in the following we will place emphasis on parameters with a high correlation to the AMOC strength or with the AMOC changes.

Density structure

All processes maintaining the density distribution in the water column are potentially important in steering the AMOC. Although virtually all models simulate a significant weakening of the AMOC under global warming conditions (Fig. 2), the reasons for changes and resulting feedback mechanisms in the individual models may differ, which is eventually reflected in a large model spread. In the 20th century runs, the simulated spatial and temporal distribution of the modeled temperature and salinity fields largely differ from model to model. Furthermore as mentioned above, the models suffer from large biases (e.g., Schneider et al. 2007).

The CMIP3 A1B (Fig 5a) and CMIP5 RCP4.5 (Fig. 5d) ensemble-mean projected changes in density, averaged zonally across the Atlantic, both show a strong reduction at the ocean surface, generally weakening with depth. The strongest surface density reduction occurs north of 40°N, with a secondary minimum near the Equator. The density signal penetrates relatively deep into the Arctic Ocean. In the Southern Hemisphere mid-latitudes near 45°S, the mean profiles show a strongly reduced density of the water column down to 1000 m depth. For some depth levels in CMIP5 RCP4.5, the Southern Hemisphere decrease in density is even larger than in the Arctic.

The impact on the density field through changes in temperature and salinity changes are also separated. The temperature effect dominates in the tropics and subtropics (Fig. 5b and 5e), where it strongly reduces the density. Salinity on the other hand tends to enhance the density (Fig. 5c and 5f). A very strong salinity-induced increase in density is located around 30°N extending to a depth of about 1000 m. At higher latitudes, especially in the Arctic region, the models consistently project a strong salinity-induced reduction in density within the upper 1000 m. The pattern in the salinity contribution to the density change might lead to an intensified meridional freshwater transport from the subtropics to the mid- and high latitudes, especially in the Northern Hemisphere. Enhanced sea ice melt and stronger river runoff into the subpolar North Atlantic and into the Arctic basin are also important in this context.

The largest uncertainties in the CMIP3 A1B projections of the density profiles (Fig. 6a and 6d) are located in the mid-latitude North Atlantic and Arctic with largest values close to the surface. Clearly, the overwhelming contribution to the total uncertainty in the projected density originates from the model uncertainty (Fig. 6b and 6e). By separating the model uncertainty in the density projections into a thermal- and a saline-driven part, it becomes also clear that the latter explains the major fraction of the model uncertainty, especially in the Arctic (Fig. 6c and 6f). The results concerning the density changes from CMIP3 are basically confirmed by those from CMIP5, with the caveat that the changes in CMIP5 tend to be somewhat weaker. Some of this difference could be due to weaker radiative forcing of the RCP4.5 scenario used in CMIP5 compared to the A1B scenario in CMIP3.

We now turn to the salinity projections themselves. The model uncertainty and the signal-to-noise ratios for both the CMIP3 and CMIP5 ensembles are estimated using the A1B and RCP4.5 scenarios (Fig. 7). Consistent with the salinity contribution to the density uncertainty (Fig. 6c and 6f), the uncertainty in the salinity projections obtained from CMIP3 shows the largest uncertainties in the mid-latitude North Atlantic and in the Arctic (Fig. 7a and 7c). The uncertainty of the salinity projections obtained from the CMIP5 ensemble is much reduced compared to that calculated from the CMIP3 models. In the CMIP3 ensemble, a well distinct region of high signal-to-noise ratio in the salinity projections is located in the region 20°N-40°N within the upper 700 m centered at a depth of about 300 m (Fig 7b). In the CMIP5 ensemble, a similar pattern is found (Fig. 7d). However, the maximum values of the signal-to-noise ratio are somewhat smaller than in CMIP3. Still, the area where it exceeds unity is larger than in CMIP3. A gain in confidence is seen in a narrow region around 40°N below 700 m. Further regions of enhanced signal-to-noise ratio in CMIP5 are found in the Southern Hemisphere at 0°-20°S and south of 40°S, approximately in the upper 200 m. We conclude that the model uncertainty determines the uncertainty in the density projections by the end of the 21st century, and that the uncertainty in the salinity projections is most relevant to the uncertainty in the density projections. In this study, we focus on the spread of model projections. Our results by no means imply that temperature changes are unimportant for the future evolution of the AMOC, but they appear to play a secondary role for the model uncertainty.

Freshwater budget

We next investigate the projections for the freshwater flux integrated over the Arctic (WFO_{Arctic}). In the CMIP5 ensemble, the projected changes in WFO_{Arctic} are anti-correlated with the changes in the AMOC index at 30°N (Table 3: r_{diff} = -0.68). The projected mean WFO_{Arctic} features some "outliers", which does not allow drawing reliable conclusions. There also is a strong anti-correlation between mean WFO_{Arctic} and the meridional density gradient (Table 4: $r_{historical}$ = -0.62 and $r_{RCP4.5}$ = -0.48). The projections of WFO_{Arctic} under the A1B (CMIP3) and RCP4.5 (CMIP5) scenarios both show a negative ensemble-mean trend (Fig. 8a and 8d), which leads to a freshening of the Arctic. However, the spread among individual models is large. In the CMIP5 projections (Fig. 8e), the model uncertainty is remarkably reduced compared to CMIP3 (Fig. 8b). This improvement could be caused by the higher complexity of the CMIP5 models that among others employ higher resolution. As a consequence, small-scale processes influencing evaporation, precipitation, river runoff, and/or sea ice can be more realistically simulated. Consistent with this, the signal-to-noise ratio (Fig. 8c and 8f) is larger in CMIP5, but it does not exceed 1.2. Uncertainty in freshwater flux affects the surface salinity in the Arctic and also remote regions by advection. The large uncertainty in surface salinity north of 40°N (Fig. 7) is at least partially explained by the highly uncertain freshwater budget. However, the projected changes in WFO_{Arctic} and in MDD (for 2070-2100 relative to 1970-2000) are not significantly correlated in the CMIP5 ensemble (Table 4: $r_{diff.}$ = -0.03), underscoring the complexity of freshwater processes in the climate models.

Subpolar Gyre index

Our results suggest that the processes in the northern North Atlantic are most important for the model uncertainties in the AMOC. This is equally confirmed by both CMIP3 and CMIP5. Therefore, our following analysis on the subpolar gyre (SPG) index is only based on the CMIP5 model ensemble. The models project an ensemble-mean reduction in the SPG index until 2100 in both scenarios (RCP4.5 and RCP8.5). The SPG index during the reference period (1970-2000) is 42.3 Sv, with a projected weakening until 2090-2100 of 10.6 Sv in RCP4.5 and 13.8 Sv in RCP8.5, i.e. a reduction of about 25% and 33%, respectively. The SPG and the AMOC indices are highly correlated across the model ensemble (Table 3: $r_{historical}$ = 0.87 and $r_{RCP4.5}$ = 0.88). However, the correlation between the projected changes of these two periods is weak ($r_{diff.}$ = 0.17). The large model spread of the SPG projection (Fig. 9a) results in high model uncertainty, which is much higher than the internal variability and scenario uncertainty (Fig. 9b). This is reflected in a signal-to-noise ratio less than unity during the entire 21st century (Fig. 9c). Therefore, a weakening of the SPG in the ensemble-mean is not significant, due to the large model uncertainty, which is possibly also affecting the AMOC strength.

The SPG index is obtained from the barotropic streamfunction, which can be split into a wind-driven flat-bottom Sverdrup transport and into a bottom pressure torque-driven transport (Greatbatch et al. 1991). We compute the uncertainties of the flat-bottom Sverdrup transport to evaluate the importance of wind stress projections in generating this high model uncertainty in the SPG. We find that model uncertainty for the total barotropic streamfunction (Fig. 10a) is much larger than for the flat-bottom Sverdrup transport (Fig. 10b). Therefore, we eliminate wind stress as a potential source for high model uncertainty in the SPG. The remaining potential source is the bottom pressure torque, which depends on bottom pressure (vertically integrated density) and on bottom topography. We conclude that model differences in density projections and potentially also the different spatial representations of the bathymetry are responsible for the high uncertainty in the SPG index projections. In fact, we find that models with a higher vertical resolution tend to simulate a stronger SPG and also a stronger weakening over the 21st century (for details see the supplementary material).

4. Summary and discussion

We have investigated the Atlantic Meridional Overturning Circulation (AMOC) projections for the 21st century obtained from the CMIP3 and CMIP5 ensembles. The CMIP5 model projections indicate a weakening of the AMOC of approximately 25% by the end of the 21st century, in agreement with the CMIP3 projections. However, the spread in CMIP5 AMOC projections is substantially larger than that in CMIP3. The model uncertainty is by far the largest contribution to the total AMOC projection uncertainty in both model ensembles. Nevertheless, by investigating the AMOC index at 30°N to compute the signal-to-noise ratio in the subtropics, which is based on the 90%-confidence level, we find that it is sufficiently large to detect an anthropogenic AMOC signal by 2030 in both CMIP3 and CMIP5. The signal-to-noise ratio is less favorable in the mid-latitude North Atlantic, which was inferred by investigating the AMOC index at 48°N.

At lead times of several decades and longer, the model uncertainty becomes much larger than the scenario uncertainty - even toward the end of the 21st century. In contrast to this, the globally averaged surface air temperature uncertainties are at these long lead times dominated by scenario uncertainty (Hawkins and Sutton 2009). Finally, we conclude that the AMOC projection uncertainty due to internal variability is unimportant at lead times beyond a few decades. Likewise, the uncertainty originating from mechanical forcing of the AMOC by atmospheric wind stress is insignificant in comparison to other sources of uncertainties. Thus, the AMOC model uncertainty appears to be dominated by the model uncertainty in projecting the oceanic density structure. The uncertainty in the projection of the density increases with latitude and is particularly strong in the subpolar North Atlantic and in the Arctic. The model uncertainties in the salinity projections explain most of the uncertainty that is found in the density projections. Salinity uncertainty in turn might be caused by uncertainties arising from freshwater flux and gyre-strength projections. The latter is important, because the strength of the SPG influences the salt advection into the regions of deep water formation. As in the salinity projections, the freshwater flux and gyre-strength projections depict large uncertainties in high latitudes. This could possibly be a reason for the large uncertainty in projecting the 21st century AMOC. Given our incomplete understanding of the AMOC, making a quantitative assessment of AMOC changes remains a challenge. Nevertheless, we can conclude that model improvements that affect the density structure in the North Atlantic will lead to a more reliable AMOC projection.

Acknowledgements:

We acknowledge the World Climate Research Programme's Working Group on Coupled Modelling, which is responsible for CMIP, and we thank the climate modeling groups for producing and making available their model output. For CMIP the U.S. Department of Energy's Program for Climate Model Diagnosis and Intercomparison (PCDMI) provides coordinating support and led development of software infrastructure in partnership with the Global Organization for Earth System Science Portals. This work was supported by the North Atlantic and the RACE Project of BMBF (grant agreement no. 03F0651B) and the European Union FP7

NACLIM project (grant agreement no. 308299). N.K. acknowledges support from the Deutsche Forschungsgemeinschaft under the Emmy Noether-Programm (grant KE 1471/2-1) and the NFR EPOCASA project (grant 229774/E10).

Conflict of Interest:

The authors declare that they have no conflict of interest.

References:

Ba J, Keenlyside NS, Latif M, Park W, Ding H, Lohmann K, Mignot J, Menary M, Otterå OH, Wouters B, Salas y Melia D, Oka A, Bellucci A, Volodin E (2014) A multi-model comparison of Atlantic multidecadal variability. Clim Dyn 43:2333–2348

Collins M, Knutti R, Arblaster J, Dufresne J-L, Fichefet T, Friedlingstein P, Gao X, Gutowski WJ, Johns T, Krinner G, Shongwe M, Tebaldi C, Weaver AJ, Wehner M (2013) Long-term Climate Change: Projections, Commitments and Irreversibility. In: Stocker TF, Qin D, Plattner G-K, Tignor M, Allen SK, Boschung J, Nauels A, Xia Y, Bex V, Midgley PM (eds) Climate Change 2013: The Physical Science Basis. Contribution of Working Group I to the Fifth Assessment Report of the Intergovernmental Panel on Climate Change, Cambridge University Press, Cambridge, United Kingdom and New York, NY, USA

Cunningham SA, Kanzow T, Rayner D, Baringer MO, Johns WE, Marotzke J, Longworth HR, Grant EM, Hirschi JJ-M, Beal LM, Meinen CS, Bryden HL (2007) Temporal Variability of the Atlantic Meridional Overturning Circulation at 26.5°N. Science 317:935-938

Danabasoglu G (2008) On Multidecadal Variability of the Atlantic Meridional Overturning Circulation in the Community Climate System Model Version 3. J Clim 21:5524-5544

de Boer AM, Gnanadesikan A, Edwards NR, Watson AJ (2010) Meridional Density Gradients Do Not Control the Atlantic Overturning Circulation. J Phys Oceanogr 40:368–380

Delworth T, Manabe S, Stouffer RJ (1993) Interdecadal Variations of the Thermohaline Circulation in a Coupled Ocean-Atmosphere Model. J Clim 6:1993-2011

Delworth TL, Zeng F (2012) Multicentennial variability of the Atlantic meridional overturning circulation and its climatic influence in a 4000 year simulation of the GFDL CM2.1 climate model. Geophys Res Lett 39:L13702

Dickson RR, Brown J (1994) The production of North Atlantic Deep Water: Sources, rates, and pathways. J Geophys Res 99:12319–12341

Ganachaud A, Wunsch C (2003) Large-Scale Ocean Heat and Freshwater Transports during the World Ocean Circulation Experiment. J Clim 16:696-705

Gnanadesikan A (1999) A Simple Predictive Model for the Structure of the Oceanic Pycnocline. Science 283:2077-2079

Gulev SK, Latif M, Keenlyside N, Park W, Koltermann KP (2013) North Atlantic Ocean control on surface heat flux on multidecadal timescales. Nature 499:464-467

Greatbatch RJ, Fanning AF, Goulding AD, Levitus S (1991) A Diagnosis of Interpentadal Circulation Changes in the North Atlantic. J Geophys Res 96:22009-22023

Hawkins E, Sutton R (2009) The potential to narrow uncertainty in regional climate predictions. Bull Am Meteorol Soc 90:1095-1107

Hawkins E, Sutton R (2011): The potential to narrow uncertainty in projections of regional precipitation change. Clim Dyn 37:407-418

Knight JR, Allan RJ, Folland CK, Vellinga M, Mann ME (2005) A signature of persistent natural thermohaline circulation cycles in observed climate. Geophys Res Lett 32:L20708

Kuhlbrodt T, Griesel A, Montoya M, Levermann A, Hofmann M, Rahmstorf S (2007) On the driving processes of the Atlantic meridional overturning circulation. Rev Geophys 45:1–32

Latif M, Keenlyside NS (2011) A Perspective on Decadal Climate Variability and Predictability. Deep Sea Res II 58:1880-1894

Latif M, Roeckner E, Botzet M, Esch M, Haak H, Hagemann S, Jungclaus J, Legutke S, Marsland S, Mikolajewicz U, Mitchell J (2004) Reconstructing, Monitoring, and Predicting

Multidecadal-Scale Changes in the North Atlantic Thermohaline Circulation with Sea Surface Temperature. J Clim 17:1605-1614

Masson D, Knutti R (2011) Climate model genealogy. Geophys Res Lett 38:L08703

McCarthy G, Frajka-Williams E, Johns WE, Baringer MO, Meinen CS, Bryden HL, Rayner D, Duchez A, Roberts C, Cunningham SA (2012) Observed interannual variability of the Atlantic meridional overturning circulation at 26.5°N. Geophys Res Lett 39:L19609Mecking JV, Keenlyside NS, Greatbatch RJ (2014) Stochastically-forced multidecadal variability in the North Atlantic: a model study. Clim Dyn 43: 271-288

Meehl GA, Covey C, Delworth T, Latif M, McAvaney B, Mitchell JFB, Stouffer RJ, Taylor KE (2007a) The WCRP CMIP3 multi-model dataset: A new era in climate change research. Bull Am Meteorol Soc 88:1383-1394

Meehl GA, Stocker TF, Collins WD, Friedlingstein P, Gaye AT, Gregory JM, Kitoh A, Knutti R, Murphy JM, Noda A, Raper SCB, Watterson IG, Weaver AJ, Zhao Z-C (2007b) Global Climate Projections. In: Solomon S, Qin D, Manning M, Chen Z, Marquis M, Averyt KB, Tignor M, Miller HL (eds) Climate Change 2007: The Physical Science Basis. Contribution of Working Group I to the Fourth Assessment Report of the Intergovernmental Panel on Climate Change, Cambridge University Press, Cambridge, United Kingdom and New York, NY, USA

Park W, Latif M (2008) Multidecadal and Multicentennial Variability of the Meridional Overturning Circulation. Geophys Res Lett 35:L22703

Park W, Latif M (2012) Atlantic Meridional Overturning Circulation response to idealized external forcing. Clim Dyn 39:1709-1726

Park T, Park W, Latif M (2016) Correcting North Atlantic Sea Surface Salinity Biases in the Kiel Climate Model: Influences on Ocean Circulation and Atlantic Multidecadal Variability. Clim Dyn, in press

Roberts CD, Jackson L, McNeall D (2014) Is the 2004–2012 reduction of the Atlantic meridional overturning circulation significant? Geophys Res Lett 41:3204–3210

Robson J, Hodson D, Hawkins E, Sutton R (2014) Atlantic overturning in decline? Nature 7:2-3

Schmittner A, Latif M, Schneider B (2005) Model projections of the North Atlantic thermohaline circulation for the 21st century assessed by observations. Geophys Res Lett 32:L23710

Schneider B, Latif M, Schmittner A (2007). Evaluation of different methods to assess model projections of the future evolution of the Atlantic Meridional Overturning Circulation. J Clim 20:2121-2132

Shakespeare CJ, Hogg AM (2012) An Analytical Model of the Response of the Meridional Overturning Circulation to Changes in Wind and Buoyancy Forcing. J Phys Oceanogr 42:1270-1287

Sijp, WP, Bates M, England MH (2006) Can isopycnal mixing control the stability of the thermohaline circulation in ocean climate models? J Clim 19:5637-5651

Sijp, WP, Gregory JM, Tailleux R, Spence P (2012) The Key Role of the Western Boundary in Linking the AMOC Strength to the North-South Pressure Gradient. J Phys Oceanogr 42:628-643

Smeed DA, McCarthy GD, Cunningham SA, Frajka-Williams E, Rayner D, Johns WE, Meinen CS, Baringer MO, Moat BI, Duchez A, Bryden HL (2014) Observed decline of the Atlantic meridional overturning circulation 2004-2012. Ocean Sci 10:29–38

Srokosz M, Baringer M, Bryden H, Cunningham S, Delworth T, Lozier S, Marotzke J, Sutton R (2012) Past, present and future change in the Atlantic meridional overturning circulation. Bull Am Meteorol Soc 93:1663-1676

Stommel H (1961) Thermohaline convection with two stable regimes of flow. Tellus 13(2):224-230

Sutton RT, Hodson DLR (2005) North Atlantic Forcing of North American and European Summer Climate. Science 309:115-118

Taylor KE, Stouffer RJ, Meehl GA (2012) An Overview of CMIP5 and the experiment design. Bull Am Meteorol Soc 93:485-498

Thorpe RB, Gregory JM, Johns TC, Wood RA, Mitchell JFB (2001) Mechanisms determining the Atlantic thermohaline circulation response to greenhouse gas forcing in a non-flux-adjusted coupled climate model. J Clim 14:3102–3116

Visbeck M, Chassignet EP, Curry R, Delworth T, Dickson B, Krahmann G (2003) The ocean's response to North Atlantic Oscillation variability. In: Hurrell JW, Kushnir Y, Ottersen G, Visbeck M (eds) The North Atlantic Oscillation: Climatic Significance and Environmental Impact, Geophysical Monograph Series, American Geophysical Union, Washington DC, pp 113-145

Wang C, Zhang L, Lee S, Wu L, Mechoso CR (2014) A global perspective on CMIP5 climate model biases. Nat Clim Change 4:201-205

Yip S, Ferro CAT, Stephenson DB, Hawkins E (2011) A simple, coherent framework for partitioning uncertainty in climate predictions. J Clim 24:4634-4643

Zhang R, Delworth TL (2006) Impact of Atlantic multidecadal oscillations on India/Sahel rainfall and Atlantic hurricanes. Geophys Res Lett 33:L17712

Tables

Table 1

CMIP3	AMOC			Salinity	Pot. T.	WFO	M_y
	A1B	A2	B1	A1B			
BCCR-BCM2.0	X	X	X	X	X		
CGCM3.1(T47)	X	X	X	X	X	X	X
CGCM3.1(T63)	X			X	X	X	X
CNRM-CM3	X			X	X	X	X
CSIRO-Mk3.0	X	X		X	X	X	X
CSIRO-Mk3.5	X	X	X	X	X	X	X
GFDL-CM2.0	X			X	X	X	X
GFDL-CM2.1	X	X	X	X		X	X
GISS-AOM	X		X	X	X		X
GISS-ER	X	X	X	X	X	X	X
INM-CM3.0	X	X	X			X	X
IPSL-CM4	X	X	X	X	X		X
MIROC3.2(hires)	X		X	X	X		X
MIROC3.2(medres)	X	X	X	X	X	X	X
MIUB-ECHO-G	X	X	X	X	X	X	X
MPI-ECHAM5	X	X	X	X	X	X	X
MRI-CGCM2.3.2a	X	X	X	X	X	X	X
NCAR-CCSM3	X						X
NCAR-PCM1	X			X	X		X
UKMO-HadCM3	X			X	X	X	X

Table 1 Models of CMIP3. The compiled dataset for the variables AMOC (Atlantic Meridional Overturning Circulation), salinity, potential temperature, WFO (freshwater flux), and M_y (northward Ekman transport). Scenarios for the 21st century are marked in addition to the 20C3M scenario.

Table 2

CMIP5	AMOC	Salinity	Pot. Temp.	WFO	Ψ	τ
	RCP45 & RCP85	RCP45			RCP45 & RCP85	
ACCESS1.3	X	X	X	X		
BCC-CSM1.1		X	X			
CanESM2	X	X	X		X	X
CCSM4	X	X	X		X	X
CESM1-BGC	X	X	X		X	X
CESM1-CAM5	X	X	X		X	X
CESM1-CAM5.1,FV2	X					
CESM1-WACCM	X	X	X		X	X
CMCC-CM		X	X	X		
CMCC-CMS		X	X	X		
CNRM-CM5	X	X	X	X	X	X
CSIRO-Mk3.6.0		X	X	X		
FGOALS-g2	X	X	X			
GFDL-CM3	X	X	X	X	X	X
GFDL-ESM2G 210		X	X	X	X	X
GFDL-ESM2M	X	X	X	X	X	X
GISS-E2-H		X	X			
GISS-E2-R		X	X			
Had-GEM2-AO		X	X			
Had-GEM2-CC		X	X	X		
Had-GEM2-ES		X	X	X		
IPSL-CM5A-LR		X	X	X		
IPSL-CM5A-MR		X	X	X		
IPSL-CM5B-LR		X	X	X		
MIROC-ESM		X	X	X		
MIROC-ESM-CHEM				X		
MIROC5	X	X	X	X		
MPI-ESM-LR	X	X	X	X	X	X
MPI-ESM-MR	X	X	X	X	X	X
MRI-CGCM3	X	X	X	X	X	X
NorESM1-M	X	X	X	X	X	X
NorESM1-ME	X	X	X	X	X	X

Table 2 Models of CMIP5. The compiled dataset for the variables AMOC (Atlantic Meridional Overturning Circulation), salinity, potential temperature, WFO (freshwater flux), Ψ (barotropic streamfunction including the subpolar gyre index), and τ (wind stress – used for computing the flat-bottomed Sverdrup transport and the northward Ekman transport). Scenarios for the 21st century are marked in addition to the historical scenario.

Table 3

	AMOC		
	1970-2000 (historical)	2070-2100 (RCP4.5)	diff.
H^2	**0.52**	**0.54**	**0.51**
MDD 74°N – 30°S	**0.75**	**0.86**	**0.55**
MDD$_{sal}$		**0.83**	**0.60**
MDD$_{temp}$		**0.65**	**-0.56**
H^2 MDD	**0.72**	**0.82**	**0.64**
WFO$_{Arctic}$	-0.53	-0.13	**-0.68**
WFO$_{subpolar}$	0.43	**-0.66**	0.25
WFO$_{Nordic\ Seas}$	**0.78**	0.51	**0.58**
WFO$_{30\text{-}50N}$	**-0.81**	**-0.65**	0.45
WFO$_{trop.\ NA}$	**-0.85**	**-0.8**	0.32
Ekman transport (50°S, 70°W-25°E)	-0.03	-0.16	-0.12
Pycnocline depth (20°N-20°S)	**0.45**	0.26	-0.1
ZDD (30°N, 70°W-20°W)	**0.63**	**0.62**	0.16
Subpolar Gyre index	**0.87**	**0.88**	0.17
Subtropical Gyre index	0.08	-0.03	**0.61**

Table 3 Correlations between different parameters and the Atlantic Meridional Overturning Circulation (AMOC) index at 30°N in the CMIP5 model ensemble. Correlation coefficients are given in three columns. The first is related to the mean of during periods 1970-2000 (historical), the second during 2070-2100 (RCP4.5) and the third to the differences between these two periods (diff.). The parameters used in the table are: the squared depth of the stream function (H^2); the meridional density difference (MDD) between 74°N and 30°S down to 1400m depth and averaged across the Atlantic; the temperature contribution to the MDD change computed using the salinity profile of the years 1970-2000 (MDD$_{temp}$) and the salinity contribution using the temperature profile of the years 1970-2000 (MDD$_{sal}$); the freshwater flux into the Arctic basin including the Barents Sea and Kara Sea region (WFO$_{Arctic}$); the freshwater flux into Atlantic ocean between 50°N and 65°N excluding the Norwegian Sea (WFO$_{subpolar}$); the freshwater flux into the Norwegian Sea, Greenland Sea and Iceland Sea (WFO$_{Nordic\ Seas}$); the freshwater flux into the Atlantic between 30°N and 50°N (WFO$_{30\text{-}50N}$); the freshwater flux into the Atlantic between 0° and 30°N (WFO$_{trop.\ NA}$); the Ekman transport at 50°S in the Atlantic sector (70°W-25°E); the pycnocline depth according to Gnanadeskian (1999); the zonal density difference (ZDD); the Subpolar Gyre index (the minimum in the barotropic streamfuction within the area 60°-15°W / 45°-65°N multiplied by -1); the Subtropical Gyre index (the maximum

in the barotropic streamfuction within the area 80°-40°W / 15°-45°N). Bold numbers are significant at the 90%-confidence level. The critical correlation coefficient varies because a different number of models was used depending on the variables.

Table 4

	MDD		
	1970-2000 (historical)	2070-2100 (RCP4.5)	diff.
H^2	**0.43**	**0.54**	0.04
WFO_{Arctic}	**-0.62**	**-0.48**	-0.03
$WFO_{subpolar}$	0.08	-0.40	-0.38
$WFO_{Nordic\ Seas}$	**0.44**	0.39	0.06
$WFO_{30\text{-}50N}$	**-0.77**	**-0.71**	-0.10
$WFO_{trop.\ NA}$	0.02	-0.01	0.32

Table 4 Correlations analogous to Table 3 but for the meridional density difference (MDD) between 74°N and 30°S down to 1400m depth instead of the Atlantic Meridional Overturning Circulation (AMOC) index. Bold numbers are significant at the 90%-confidence level. The critical correlation coefficient varies because a different number of models was used depending on the variables.

Figures

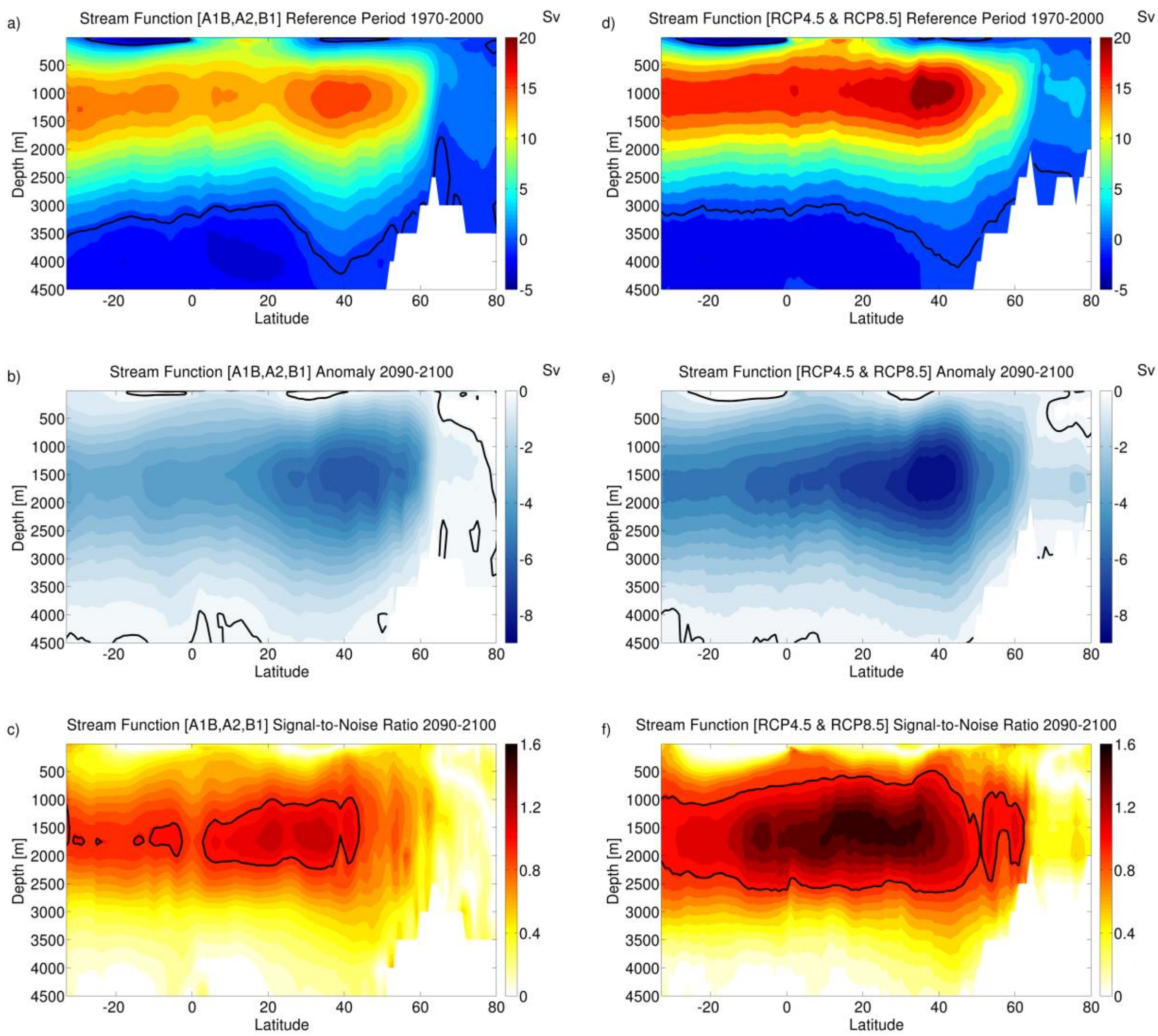

Fig. 1 The Atlantic meridional overturning streamfunction for CMIP3 and CMIP5 from the models listed in Table 1 and Table 2. Panels **(a-c)** summarizes the results for CMIP3 (20C3M, SRES A1B, A2 and B1 scenarios), and the panels (**d**-**f**) provide the results for CMIP5 (historical, RCP4.5 and RCP8.5 scenarios). (**a**, **d**) ensemble-mean overturning streamfunction (Sv = 10^6 m³/s) for the reference period year 1970-2000. (**b**, **e**) anomaly by 2090-2100 relative to the reference period 1970-2000. (**c**, **f**) signal-to-noise ratio with the 90%-confidence limit given by the black contour. Please note the different scales in the color bars

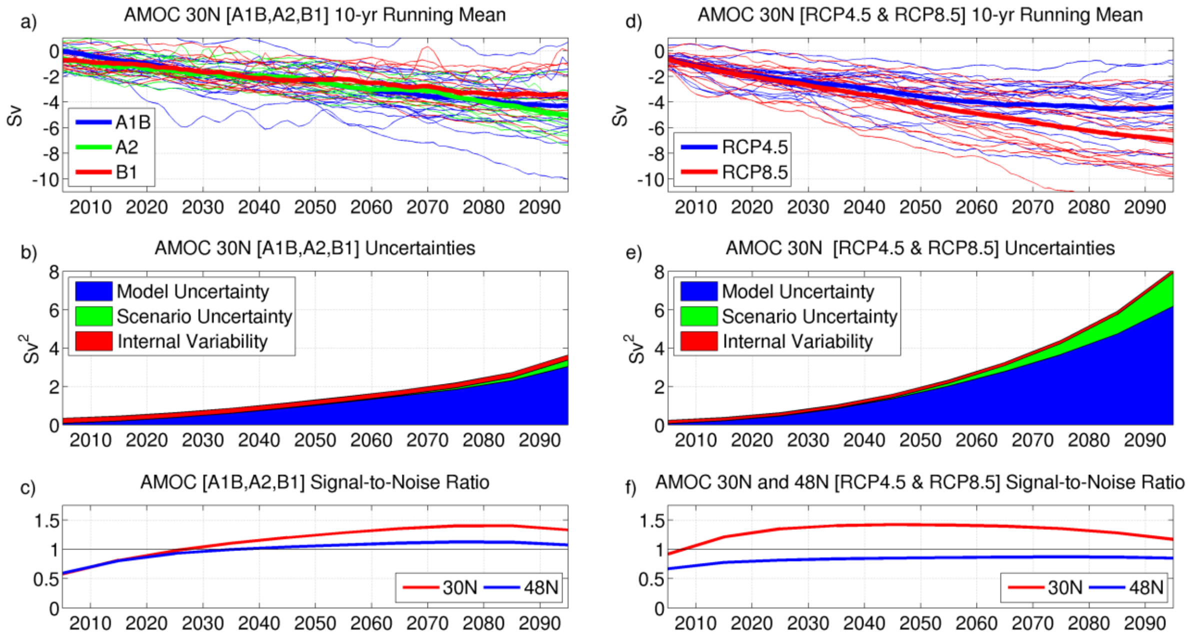

Fig. 2 Sources of the uncertainties in projections of the AMOC until 2100. a-c: CMIP3 (SRES A1B, A2 and B1). (**d-f**) CMIP5 (RCP4.5 and RCP8.5). (**a**) and (**d**): AMOC long-term changes of the individual models at 30°N; the 10-year running mean is presented (the climate mean of the reference period 1970-2000 has been removed). (**b**) and (**e**): individual absolute uncertainties of the AMOC projections (Sv^2) at 30°N. (**c**) and (**f**): signal-to-noise ratio for the AMOC changes at 30°N (red) and 48°N (blue)

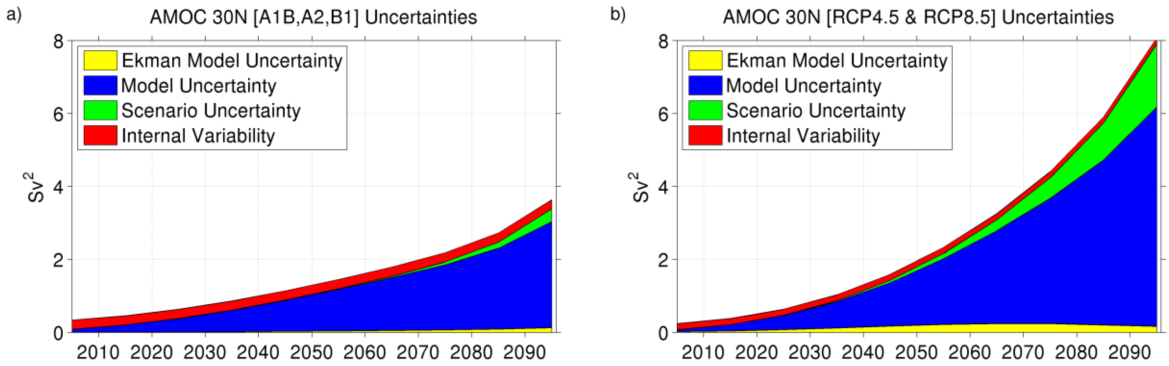

Fig. 3 Absolute uncertainties of the AMOC (Atlantic Meridional Overturning Circulation) projections at 30°N in CMIP3 (Sv = 10^6 m³/s). The figures are the same as Figs. 2b and 2e except that they include the contribution of the wind-driven meridional Ekman transport to the model uncertainty (yellow). (**a)** for CMIP3 with the scenarios A1B, A2, and B1. (**b**) for CMIP5 with the scenarios RCP4.5 and RCP8.5

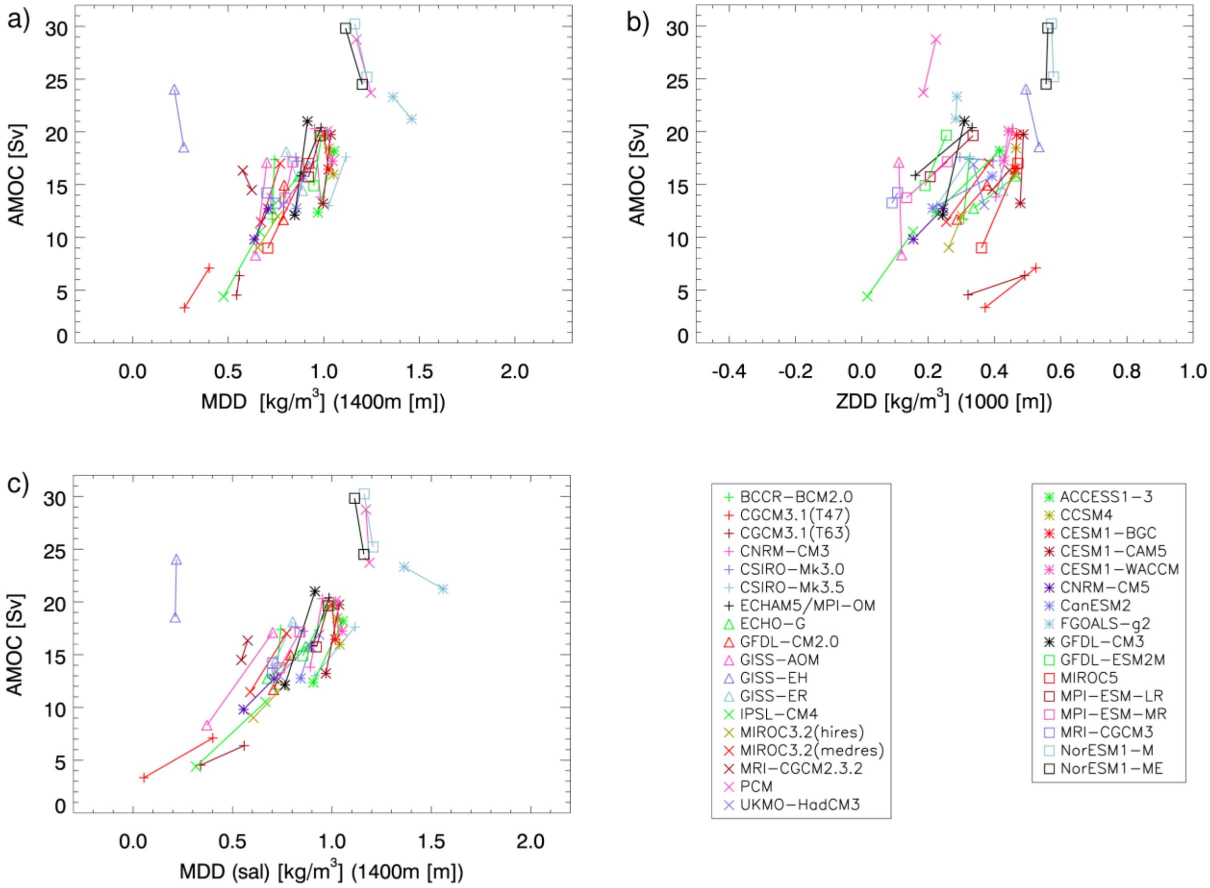

Fig. 4 AMOC index at 30°N and (**a**) meridional density difference (MDD) between 74°N and 30°S, (**b**) zonal density difference (ZDD) at 30°N. (**c**): same as (**a**) but the 21st century density includes only the salinity effect, i.e. temperature profile of CMIP3 (CMIP5) has been taken from 20C3M (historical). Each symbol represents one model; the line connects the symbols for the 20C3M (historical) run averaged over 1970-2000 with the SRES A1B (RCP4.5) run averaged over 2070-2100

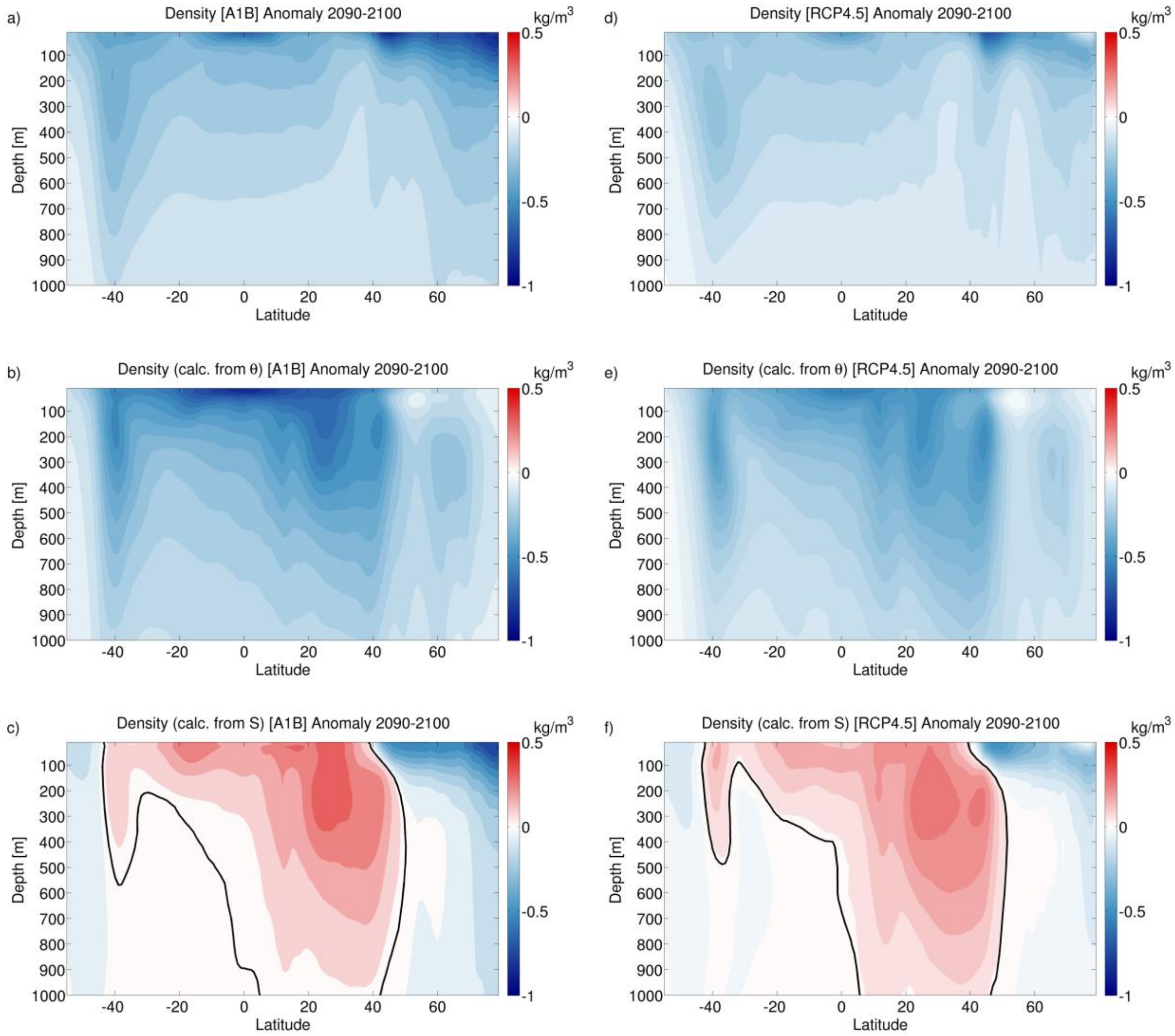

Fig. 5 Density anomaly projections for CMIP3 (**a**-**c**) and CMIP5 (**d**-**f**). a and d: The Atlantic basin meridional profiles of the ensemble mean potential density anomalies 2090-2100 relative to 1970-2000. (**b**) and (**e**): density anomaly based only on the projected changes in potential temperature. (**c**) and (**f**): density anomaly based only on the projected changes in salinity

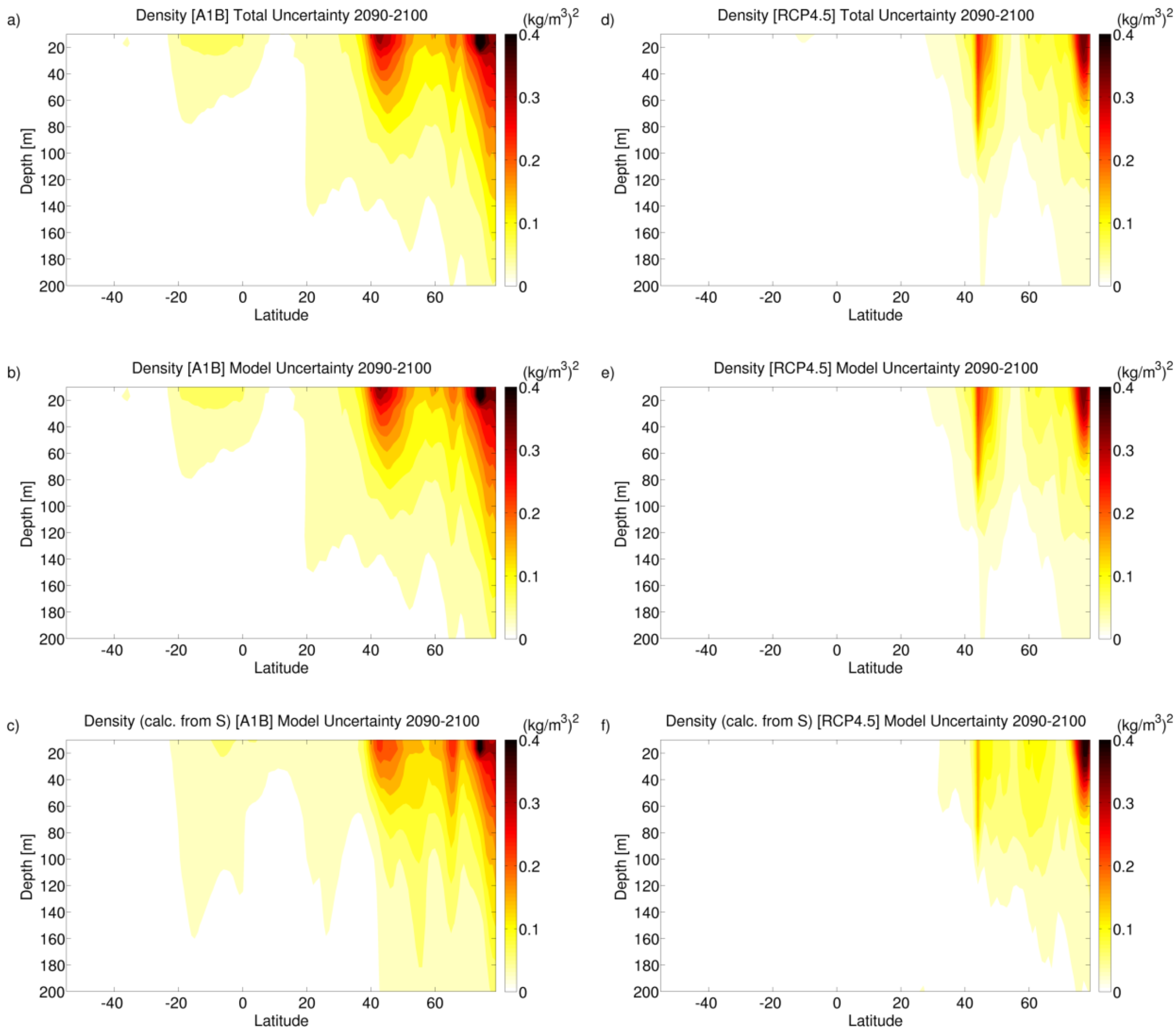

Fig. 6 Uncertainties in the density projections for CMIP3 (**a**-**c**) and CMIP5 (**d**-**f**). (**a**) and (**d**): the total uncertainties in the density projection. (**b**) and (**e**): the model uncertainty in the density projection. (**c**) and (**f**): the model uncertainty in the density projection based only on salinity projections (temperature is kept constant)

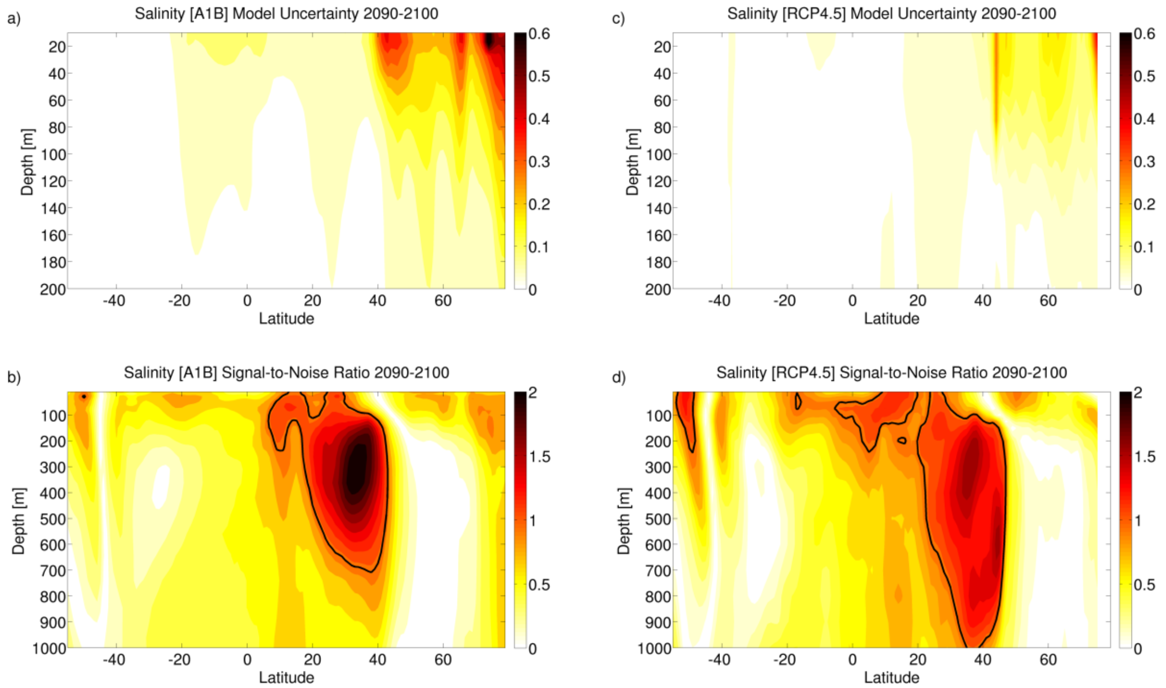

Fig. 7 Uncertainties in the salinity projection for CMIP3 (**a**-**b**) and CMIP5 (**c**-**d**). (**a**) and (**c**): the model uncertainties in the salinity projections. (**b**) and (**d**): signal-to-noise ratio with a 90%-confidence limit (ratio of 1 is given by the black contour)

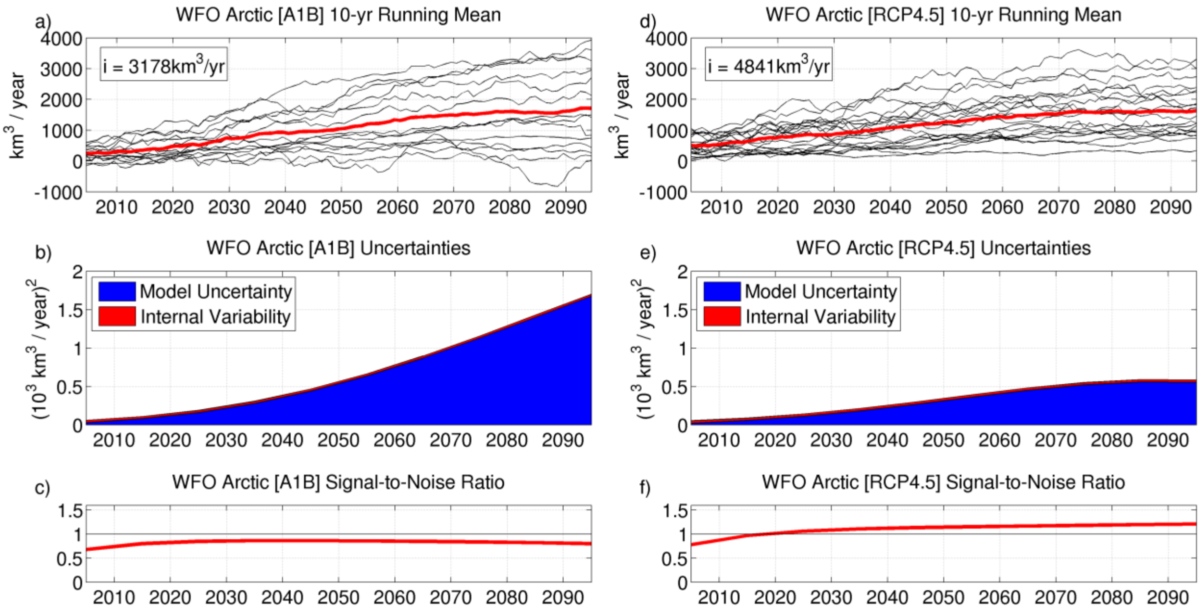

Fig. 8 Sources of uncertainty in the projection of freshwater flux anomalies into the Arctic Ocean for CMIP3 (**a-c**) and CMIP5 (**d-f**). (**a**) and (**d**): The individual model runs (black) and the ensemble-mean (thick red). A 10-year running mean is applied. The climate mean for the period 1970-2000 is removed. (**b**) and (**e**): absolute values of the model uncertainty and the internal variability. (**c**) and (**f**): signal-to-noise ratio

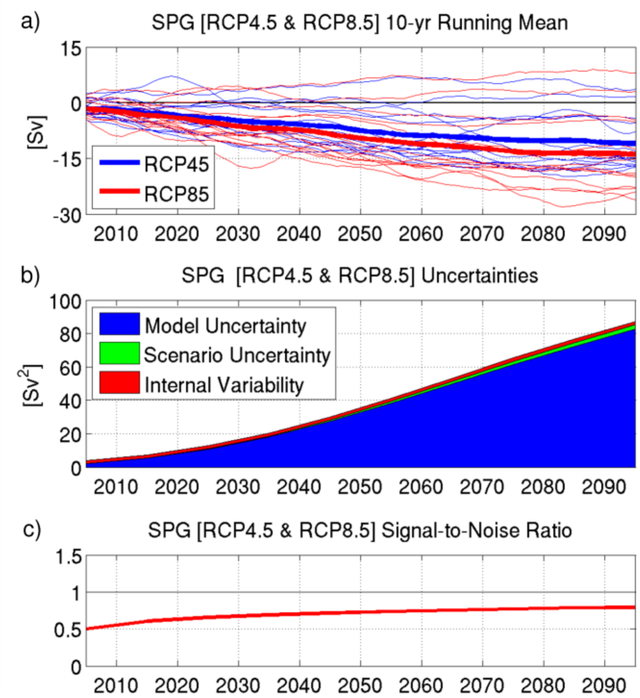

Fig. 9 Sources of uncertainty in the subpolar gyre (SPG) index projection until 2100 in the CMIP5 model ensemble using the scenarios RCP4.5 and RCP8.5. (**a**) SPG index long-term changes of the individual models; only 10-year running mean is presented (the climate mean has been removed); (**b**) individual absolute uncertainties of the SPG index projections; (**c**) signal-to-noise ratio for the SPG index changes

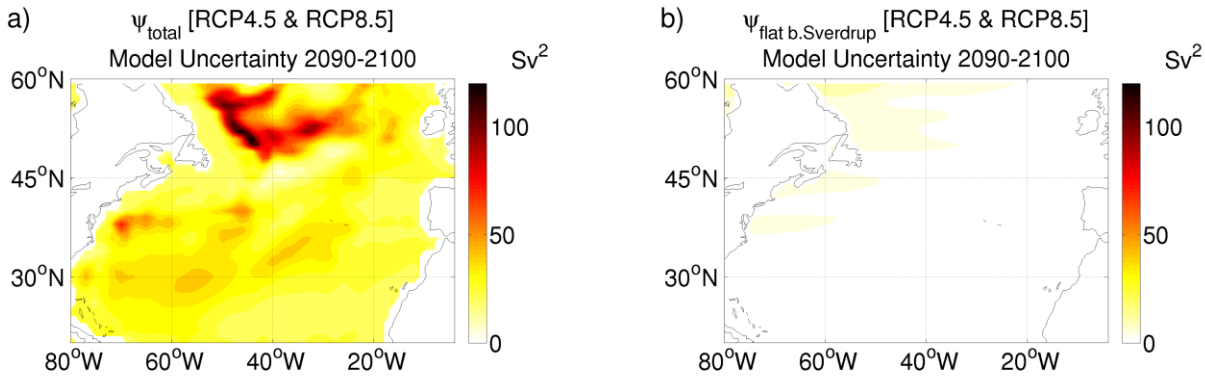

Fig. 10 Model uncertainty of the barotropic streamfunction projections of CMIP5 for 2090-2100; (**a**) for the total barotropic streamfunction from the model output and (**b**) for the flat-bottomed Sverdrup transport computed from wind stress data. The scenarios RCP4.5 and RCP8.5 are used